Article

From Localized Laser Energy Absorption to Absorption Delocalization at Volumetric Glass Modification with Gaussian and Doughnut-Shaped Pulses

Martin Zukerstein [1], Vladimir P. Zhukov [1,2,3], Yuri P. Meshcheryakov [4] and Nadezhda M. Bulgakova [1,*]

[1] HiLASE Centre, Institute of Physics ASCR, 25241 Dolni Brezany, Czech Republic; zukerstein@fzu.cz (M.Z.)
[2] Federal Research Center for Information and Computational Technologies, Novosibirsk 630090, Russia
[3] Novosibirsk State Technical University, Novosibirsk 630073, Russia
[4] Design and Technology Division, Lavrentyev Institute of Hydrodynamics SB RAS,
    Novosibirsk 630090, Russia; director@sibexplo.com
[*] Correspondence: bulgakova@fzu.cz

Abstract: Volumetric modification of transparent materials by femtosecond laser pulses is successfully used in a wide range of practical applications. The level of modification is determined by the locally absorbed energy density, which depends on numerous factors. In this work, it is shown experimentally and theoretically that, in a certain range of laser pulse energies, the peak of absorption of laser radiation for doughnut-shaped (DS) pulses is several times higher than for Gaussian ones. This fact makes the DS pulses very attractive for material modification and direct laser writing applications. Details of the interactions of laser pulses of Gaussian and doughnut shapes with fused silica obtained by numerical simulations are presented for different pulse energies and compared with the experimentally obtained data. The effect of absorbed energy delocalization with increasing laser pulse energy is demonstrated for both beam shapes, while at relatively low pulse energies, the DS beam geometry provides stronger local absorption compared to the Gaussian geometry. The implications of a DS pulse action for post-irradiation material evolution are discussed based on thermoelastoplastic modeling.

Keywords: volumetric modification; femtosecond laser pulses; laser processing; fused silica; Maxwell's equations; thermoelastoplastic modeling; laser-induced shock waves

1. Introduction

Irreversible local modification of glasses created by the impact of ultrashort laser pulses, which is manifested as an increase in the refractive index [1–5], is used in many applications based on direct writing of three-dimensional structures, such as waveguides [1,6–8], waveplates [9,10], Bragg gratings [11–13], optical memories [14–16], computer-generated holograms [17], and microfluidic devices [18,19]. From its first demonstration [1], this technique has attracted considerable attention from researchers due to its importance for existing and emerging technologies. The conventional way to perform volumetric laser processing is the use of Gaussian pulses. However, the spatially and/or temporally shaped pulses can be highly advantageous for many applications [20–24]. For example, Bessel laser beams have been shown to be much more efficient for high aspect ratio structuring of glass, as well as for drilling and cutting dielectric materials, compared to conventional Gaussian pulses [22,25–27]. Further, top-hat laser pulses can be advantageous for uniform surface processing [28,29]. Recently, via numerical modeling, we predicted that, in a given range of pulse energies, the peak absorbed energy density would be more than 10-fold higher when focusing a doughnut-shaped laser pulse inside the bulk glass than with Gaussian pulses [30]. Temporal pulse shaping has also demonstrated great potential to control material modifications, such as inverting the regular material response, resulting in a significant

refractive index increase [21]. The interaction of ultrashort laser pulses with energies sufficient for inducing local structural modification in the bulk of transparent materials is a very complicated process involving several nonlinear phenomena (self-focusing, multiphoton absorption and ionization, electron avalanche ionization, scattering of laser radiation by generated electron plasma, etc.) [31]. Despite extensive studies of this topic, the mechanisms of laser energy absorption and localization and the effects of laser beam shaping on energy localization are still not completely understood and described [25,27,31,32].

This work is focused on experimental and theoretical studies of the laser energy absorption by fused silica in volumetric modification regimes using Gaussian and doughnut-shaped (DS) femtosecond laser pulses. We investigate the evolution of the absorbed energy distribution and the plasma shielding effect in a wide range of pulse energies. The experimental studies were supported by numerical modeling of the propagation of ultrashort laser pulses in nonlinear media by axially symmetric Maxwell's equations. The experimental and numerical data are in good qualitative agreement, allowing us to reveal the trends of laser energy absorption and its delocalization with increasing beam intensity. We also discuss the possible consequences of strong laser energy localization, in the case of DS laser pulses, for material modification due to enhanced stresses and the generation of elastoplastic waves.

2. Experiment

An Astrella Ti:sapphire laser system (Coherent) was used in the experiments, providing ultrashort laser pulses with a time duration of $\tau_{\text{FWHM}} \approx 40$ fs at the central wavelength of $\lambda_0 = 800$ nm. The experimental setup consisted of several sections: an attenuator (half-wave plate and polarizer), a beam shaping section (half-wave/quarter-wave plate for polarization control, an S-waveplate for converting from Gaussian to doughnut-shaped pulses), a beam profiler (beam shape and size control), and a focusing part (objective $10\times$ magnification with numerical aperture NA = 0.25). The energy transmission experiments were performed with the same experimental settings. The energy of the transmitted pulse was measured by an energy meter behind the sample. The pulse duration was controlled by the compressor in the laser system. The irradiated samples were fused silica plates with a thickness of 1 mm. They were positioned on an xyz-stage provided that the light freely transferred through the rear side without reflection from a substrate. The laser beam was focused 200 μm below the surface of the sample. The experimental setup is shown schematically on Figure 1.
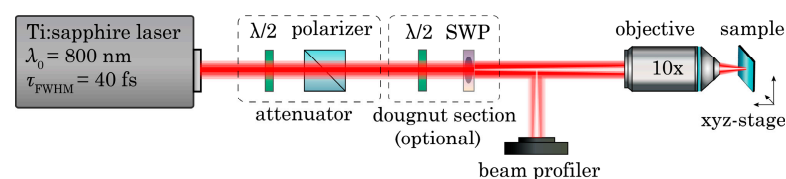
Figure 1. The scheme of the experimental setup.

Structural changes within the modified areas were examined with an optical microscope (Olympus BX43) by focusing on the plane of the laser-affected zone having the highest modification contrast. The modification level for each image was evaluated as a dimensionless quantity from the grayscale in the classical transmission imaging mode. We emphasize that the analysis of all images was performed for the same glass plate using the same setup of the microscope with the same grayscale balance to avoid misinterpretation of the optical results. We primarily aimed to investigate volumetric modification by individual laser pulses. However, the contrast of the modified areas imaged could be too weak to obtain clean, low-noise data. Thus, the modifications were studied for accumulated pulses (1; 2; 3; 5; 10; 20; and 50) acting on the same sample region. We note that the modification level in the material evolved nonlinearly with the number of applied pulses. Thus, the

modification level at multiple pulses was used as a relative quantity to compare different regimes of interaction in terms of pulse energy and beam shape.

3. Theoretical Model

Numerical simulations of the experimental conditions were performed based on nonlinear Maxwell's equations written for the complex amplitudes of the vector functions and supplemented by equations describing the excitation of electrons, their trapping, re-excitation, and oscillations in the field of the laser wave [30,33]

$$\frac{1}{c}\frac{\partial \boldsymbol{D}}{\partial t} - i\frac{\omega}{c}\boldsymbol{D} = \frac{4\pi}{c}e\rho\boldsymbol{v} + \text{rot }\boldsymbol{B} - \frac{8\pi}{c|E|^2}\hbar\omega\left(\alpha W_{\text{PI}} + \alpha_{\text{STE}}W_{\text{PI}}^{\text{STE}}\right)\boldsymbol{E}, \tag{1}$$

$$\boldsymbol{D} = n^2\left(1 + \frac{cn_2|E|^2}{4\pi}\right)\boldsymbol{E}, \tag{2}$$

$$\frac{1}{c}\frac{\partial \boldsymbol{B}}{\partial t} - i\frac{\omega}{c}\boldsymbol{B} = -\text{rot }\boldsymbol{E}, \tag{3}$$

$$\frac{\partial \rho}{\partial t} = W_{\text{PI}} + W_{\text{PI}}^{\text{STE}} + W_\sigma - \frac{\rho}{\tau_{\text{tr}}}, \tag{4}$$

$$\frac{\partial \rho_{\text{STE}}}{\partial t} = -W_{\text{PI}}^{\text{STE}} + \frac{\rho}{\tau_{\text{tr}}}, \tag{5}$$

$$i\omega\boldsymbol{v} = (e/m_e)\boldsymbol{E} + \boldsymbol{v}/\tau_c, \tag{6}$$

$$W_{\text{PI}} = W_{\text{PI0}}\left(|E|^2/E_*^2\right)^\alpha \frac{\rho_0 - \rho - \rho_{\text{STE}}}{\rho_0}, \tag{7}$$

$$W_{\text{PI}}^{\text{STE}} = W_{\text{PI0}}^{\text{STE}}\frac{\rho_{\text{STE}}}{\rho_0}\left(|E|^2/E_*^2\right)^{\alpha_{\text{STE}}}, \tag{8}$$

$$W_\sigma = \frac{e^2\tau_c|E|^2}{2m_e E_g(1+\omega^2\tau_c^2)}\frac{\rho(1-\rho/\rho_0-\rho_{\text{STE}}/\rho_0)}{(1+m/m_h)}, \tag{9}$$

$$E_g = E_{g0}\left(1 + |E|^2/\left(4E_*^2\right)\right), \tag{10}$$

$$E_* = \frac{\omega\sqrt{mE_{g0}}}{e} \tag{11}$$

Here, $\omega = 2\pi c/\lambda$ ($\lambda = 800$ nm) is the laser pulse frequency; ρ and $\boldsymbol{v}$ are, respectively, the density and the velocity of the electrons excited to the conduction band; e is the elementary charge; and W_{PI} and $W\sigma$ are the multiphoton and collisional ionization rates, respectively. We use here the value $W_{\text{PI0}} = 3.1 \times 10^{34}$ cm^{-3} s^{-1} of 6-photon ionization ($\alpha = 6$ and the band gap $E_{g0} = 9$ eV), which is derived from the Keldysh photoionization theory at relatively low intensities of the laser field. It was found that, varying the W_{PI0} value in the range from 10^{34} to 3.7×10^{34} cm^{-3} s^{-1}, the simulation results on laser energy absorption were not notably changed due to beam "self-regulation" (higher MPI rates lead to earlier electron plasma formation, resulting in earlier light scattering) [33]. The values ρ_{STE} and $W_{\text{PI}}^{\text{STE}}$ are the density and the multiphoton ionization rate of the self-trapped excitons (STEs), respectively. According to the literature [34–36], the absorption band related to the STEs in fused silica is within the range of 5–6 eV. Thus, the excitation of electrons trapped in the STE states is a 4-photon process at the wavelength of 800 nm, and we consider $\alpha_{\text{STE}} = 4$. Then, the Keldysh theory at relatively low laser fields yields for a 4-photon excitation process $W_{\text{PI}}^{\text{STE}} \approx 10^{37}$ cm^{-3} s^{-1}. For simplicity, the electron excitation from the STE states was not considered in the avalanche ionization process, as it is lower than the avalanche from the valence band. The electron collision time was taken as $\tau_c = 3/\omega$ [21]. The linear and nonlinear refractive indices of fused silica were, respectively, $n = 1.45$ and $n_2 = 2.48 \times 10^{-16}$ cm^2 W^{-1}. The reduced electron mass m was considered to be $m_e/2$, with m_e being the electron mass in a vacuum [37] and $m_h = mm_e/(m_e - m)$. The atomic density of fused silica is $\rho_0 = 6.6 \times 10^{22}$ cm^{-3}. The normalization parameter E_* was the laser

field strength at which the Keldysh parameter $\gamma = 1$. This value corresponds to intensity $I_* = c\varepsilon_0 n \,|\, E^2 \,|\, /2 = 2.74 \times 10^{13}$ W cm^{-2}. In Equation (6) for the electron velocity, the term $\partial v / \partial t$, which is much smaller than ωv, has been neglected. A series of simulations showed that this simplification does not lead to a notable difference from the modeling results presented thereafter. We assume here that the hot electrons cannot be trapped in the STE states during the acceleration stage in the strong field of the laser wave. Thus, the trapping time $\tau_{tr} = 150$ fs [38] was introduced when the electric field drops to less than $E^2 / E_*^2 < 0.01$, otherwise $\tau_{tr} = \infty$. We note that the described approach can be applied to a wide variety of bandgap materials, such as multicomponent glasses, crystalline solids, and polymers, provided that the physical and optical properties of a material are known.

Equations (1)–(11) are solved in two-dimensional (2D) geometry (the coordinates (r, z)). In the case of a radially polarized DS laser pulse, this geometry is satisfied precisely. For linearly polarized Gaussian pulses, the cylindrical symmetry of the beam propagation and, hence, of light absorption can be violated, especially at high NA [33]. The validity of the 2D approach was controlled during simulations as previously described [39]. It was found that, for the parameters used in the present simulations, the cylindrical symmetry was preserved with high accuracy. The equations are solved by a finite-difference scheme [30,40]. The initial conditions for the equations correspond to the unperturbed fused silica sample. The laser pulse starts to propagate from the boundary of the simulation region $(z, r) = (0, r)$. Its shape corresponds to the laser beam focused by a parabolic mirror [41,42]. The pulse incident on the mirror is described as

$$E_{inc} = E_0(r)\exp\left(-i\omega(t + z/c) - (t + z/c)^2/t_L^2\right). \tag{12}$$

The mirror has an aperture NA = 0.25 (the ratio of the initial unfocused beam radius w_{in} to the focal distance of the mirror), and its axis coincides with the z axis of the laser beam. In all simulations presented below, the mirror focus d was placed at the distance $z = 400$ μm, and the FWHM pulse duration was 45 fs, longer than in experiments. The deeper focus was chosen to consider possible situations in which the light absorption starts at distances greater than 200 μm from the geometrical focus, which can happen at relatively large pulse energies. However, in all the ranges of the pulse energies, notable light absorption was initiated closer than 200 μm to the focus, and the simulations result do not depend on the focus depth ≥ 200 μm in our particular case. We note that, in the case of a linearly polarized Gaussian beam, $E_0 \sim \exp(-r^2/w_{in}^2)$, while for a radially polarized DS pulse, $E_0 \sim (r/w_{in})\exp(-r^2/w_{in}^2)$. To calculate the electric field distribution, the Stratton–Chu integral technique is used [43,44].

The distribution of the absorbed laser energy density, which determines the level of modification inside the laser-irradiated material, was integrated during the laser beam propagation from the simulation start (t_0) until the laser beam left the focal zone, and further light absorption became negligible (t_1):

$$E_{ab} = \int_{t_0}^{t_1} \left(\frac{jE^* + j^*E}{4} + \alpha\hbar\omega W_{PI} + \alpha_{STE}\hbar\omega W_{PI}^{STE}\right)dt. \tag{13}$$

4. Results and Discussion

The expected result was the observation of a stronger volumetric modification in the case of the DS laser pulses, as predicted theoretically [30]. Indeed, when we apply pulses with relatively small energies $E_p \leq 16$ μJ (see Figure 2a,c), the experimental data are in agreement with this prediction (note that, in [30], $E_p \leq 2$ μJ). However, the opposite behavior was observed for the E_p values greater than16 μJ (Figure 2a,b). In this work, the calculations cover a wider range of the pulse energies than in [30], and as shown below, their results agree qualitatively with the experimental data.
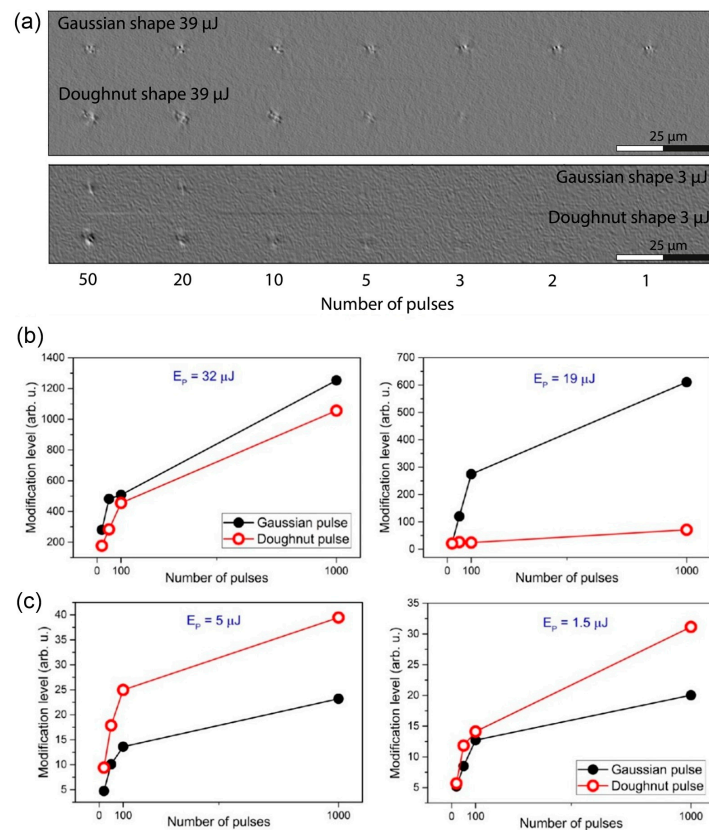
Figure 2. (**a**) Optical microscope images of volumetric modifications by Gaussian and DS laser pulses with energies of 39 and 3 μJ, respectively. (**b**) Comparison of modification levels for the Gaussian and DS laser pulses at the high E_p values of 32 and 19 μJ, respectively. (**c**) The same as in (**b**) for relatively low pulse energies of 5 and 1.5 μJ. The modification level is a dimensionless quantity evaluated from the optical microscope images of the modified areas on the planes of the highest modification contrast (the grayscale in the classical transmission imaging mode).

The peak values of the absorbed energy density E_{ab}^{peak} as a function of the pulse energy for the Gaussian and DS pulses obtained in the numerical simulations are shown in Figure 3. As mentioned above, the absorbed energy density E_{ab} plays a crucial role in material modification. According to thermodynamic considerations [45], gentle modification of fused silica in the form of compaction can take place already with single laser shots if E_{ab} exceeds ~1700 J/cm^3. If the E_{ab} value is higher than ~2400 J/cm^3, the material is locally melting, which can lead to a stronger modification, including bubble formation, which depends on E_{ab}^{peak} and associated pressure gradients. In the Gaussian case considered here (Figure 3), the E_{ab}^{peak} value increases gradually, while for the DS pulses, the absorption demonstrates a strong maximum at moderate E_p, which several times (up to 5 for E_p = 1.5 μJ) exceeds E_{ab}^{peak} of the Gaussian pulse case. However, with increasing pulse energy to ~16 μJ, the E_{ab}^{peak} values for the Gaussian and DS cases become approximately equal, and at E_p > 16 μJ, the situation overturns with the achieving of higher local absorption for the Gaussian pulses. We note that, in ref. [30], a stronger enhancement peak of E_{ab}^{peak} was reported for the DS case compared to the Gaussian one at moderate pulse energies that could be explained using more accurate boundary conditions here that better describe the tightly focused laser beams. However, the main tendency that, at a certain pulse energy range, DS pulses can lead to a stronger and more localized 3D material modification remains the same.
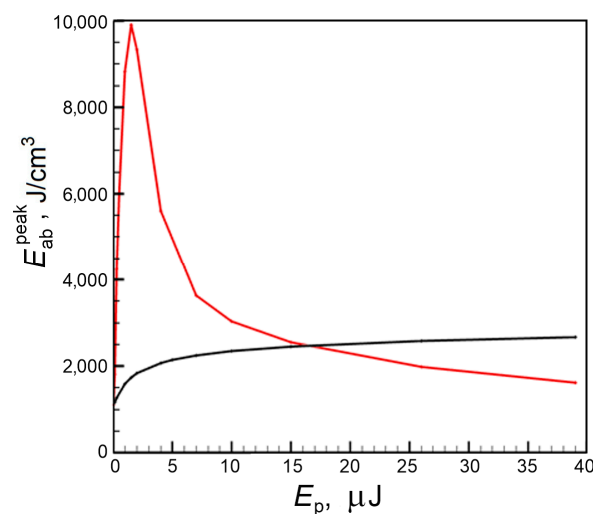
Figure 3. The peak values of the absorbed energy density as a function of the pulse energy E_p. Red and black curves correspond to the DS and Gaussian pulses, respectively.

Figure 4 presents the distributions of the absorbed laser energy density after laser beam propagation through the sample (simulation region) for the Gaussian (upper panel) and DS (bottom panel) laser pulses at the E_p values of 0.5, 1.5, 7, and 15 μJ. The laser pulse propagates from the bottom. The geometrical focus is indicated by white dashed lines. It is evident that, with increasing pulse energy, laser energy absorption starts at a greater distance before reaching the geometric focus, thus resulting in absorbed energy delocalization similar to that reported by Zavedeev et al. [46] for the case of silicon. For the Gaussian laser pulses, this process leads to the energy clamping effect [47,48]. Indeed, by increasing E_p 30 times, from 0.5 to 15 μJ, the E_{ab}^{peak} increases monotonously by slightly more than two times. The behavior of light absorption in the case of DS pulses is strongly different from the Gaussian case, as studied in detail in ref. [30]. Briefly, in the DS case, free-electron plasma generated by the pulse front in the form of a toroid scatters the remaining part of the pulse in two directions: to the periphery and to the axis. The part of the pulse converging toward the beam axis is swiftly densifying in intensity, thus overcoming the intensity clamping. However, due to the strong ionization accompanying beam collapse, the light intensity drops before reaching the axis, thus creating a hollow, highly ionized cylindrical zone. Both its length and E_{ab} in the "hot cylinder" region strongly depend on the pulse energy: the higher E_p is, the longer is the length of the "hot cylinder" is, and the lower the E_{ab}^{peak} value is (Figure 4, bottom). Thus, the absorbed energy delocalization along the way of the DS pulse shrinking upon focusing is accompanied by the effect of E_{ab} delocalization along the excited cylindrical zone.

Comparing the E_{ab} distributions for the Gaussian and DS cases, we admit that, in the first case, E_{ab}^{peak} is always located slightly before the geometric focus, while in the DS case, it shifts toward the laser with increasing pulse energy (Figure 4), which is understood from the light scattering geometry. Interestingly, in the DS case, the second maximum of E_{ab} emerges straight behind the geometric focus with enhanced E_p (Figure 4, 7 μJ and 15 μJ). This peak is explained by the filamentation of the beam. After shrinking to the focal region, the beam has still enough energy to be refocused by creating a new "hot spot", presumably assisted by interfering with light scattered from the "hot cylinder". However, the E_{ab}^{peak} value in the second absorption region is relatively small and cannot induce a notable modification compared with the peak in front of the "hot cylinder".
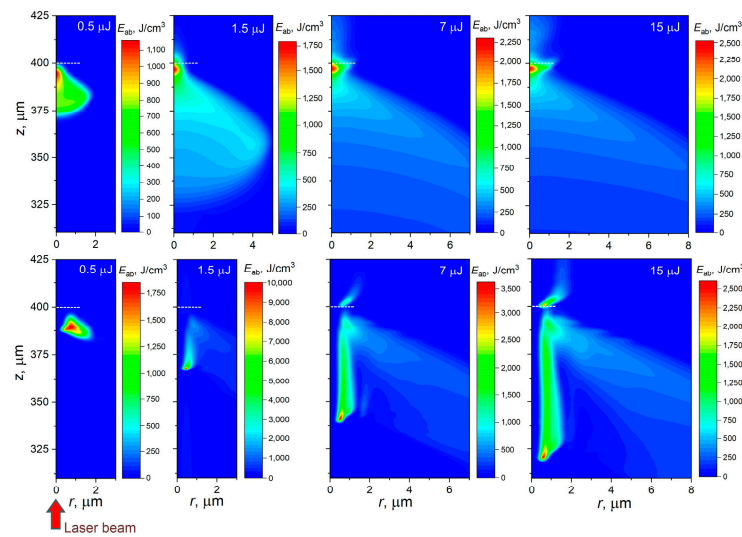
Figure 4. The absorbed energy density distributions obtained in simulations for the Gaussian (upper row) and DS laser pulses (bottom row) at different pulse energies. The pulse propagates from the bottom to the top. The geometric focus is at z = 400 µm (shown by white dashed lines).

The simulation results shown in Figures 3 and 4 are in reasonable qualitative agreement with the experimental results (Figure 2), including the overall change in the $E_{\mathrm{ab}}^{\mathrm{peak}}$ tendency from higher values at relatively low energies for the DS pulses to larger modification levels for the Gaussian laser pulses with increasing pulse energy. Thus, the model provides a well-supported explanation for the observations. This outcome indicates that the employed theory accounts adequately for the physical processes involved in the phenomenon of ultrafast laser modification of transparent materials; hence, this modeling approach is predictive. Interestingly, the measured transmitted energy has an opposite tendency, as shown in Figure 5. At low laser pulse energies, $\leq$0.6 µJ, more laser light is transmitted through the sample for the DS pulses, while at 0.6 µJ < E_{p} $\leq$ 1.5 µJ, the light transmission is measured as equal in the DS and Gaussian cases. When the beam energy approaches and exceeds 2 µJ, the Gaussian beam is transmitted slightly better (by only ~2–3%). Since the maximum local absorption of light from the DS pulses is considerably higher at relatively low energies (see, e.g., Figures 2a,c, 3 and 4), this outcome indicates much more efficient laser energy coupling compared to Gaussian pulses, representing one of the solutions on the roadmap to achieve extreme laser-processing scales [49].
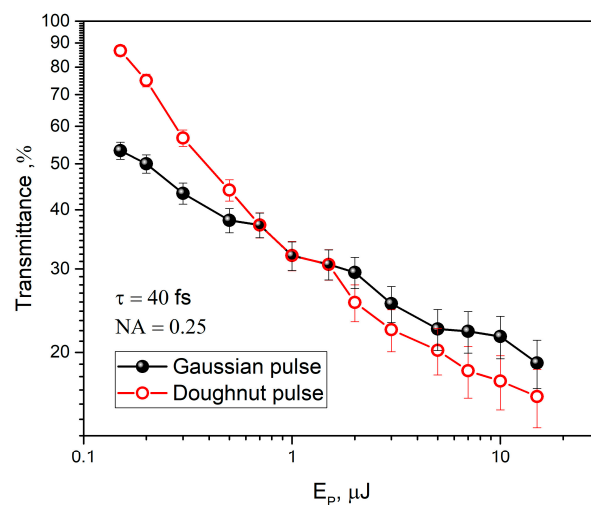
Figure 5. Experimental data on the transmitted energy of the single Gaussian (black curve) and DS (red curve) ultrashort laser pulses in the energy range E_{p} = 0.15–15 µJ.

A similar trend was found in the simulations as an evaluation of the initial beam energy minus the absorbed one. Although quantitatively, the theoretical data diverge from the measured transmittance values, at relatively low beam energies, the transmittance of the laser pulse is higher for the DS case, while with increasing beam energy, the situation reverses, demonstrating higher transmittance for the Gaussian pulses. A quantitative discrepancy between the experimental and numerical results is conditioned by several factors. First, the material parameters, such as the rates of photo- and avalanche ionization from both the ground and trapped excitonic states, are still poorly known. In addition, the photoionization rates can swiftly vary during irradiation due to the laser-induced evolution of the band structure, with possible band splitting and metallization of a dielectric in the strong field of the laser wave [50,51]. An important factor is the difference between the perfect shapes of laser beams used in modeling and the real experimental beam shapes. The difference is demonstrated in Figure 6 for the Gaussian and DS beams, where curve 1 represents the theoretical beams and curve 2 refers to the pulses used in the present experiments. Although the theoretical curves are designed to reproduce the experimental beam shapes, the evident disparities can lead to considerable differences in laser excitation given the nonlinear nature of bandgap material excitation.
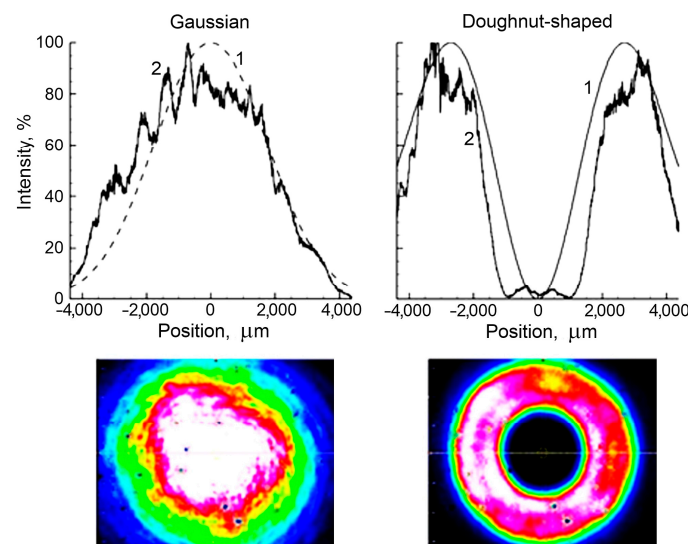
Figure 6. Top: The spatial profiles of the laser intensity of the Gaussian (**left**) and DS (**right**) laser beams before the focusing lenses. Curves 1 and, 2 correspond, respectively to the shapes used in the simulations and measured experimentally. Bottom: Laser beam cross-sectional images recorded with a laser beam profiler.

However, it must be underlined that our numerical model has proven to be a predictive tool, as it forecasted higher efficiency of laser energy coupling for DS pulses compared to Gaussian ones [30], which has been supported experimentally in this work. Here, we have also found that the model describes qualitatively well the experimentally observed tendencies in material modification in a wide range of pulse energies. We anticipate that the DS pulses upon proper shaping and focusing can be efficiently used in such applications as bringing the matter to extreme states for exploring warm dense matter and inducing implosion of the absorbed laser energy with the creation of high-pressure material phases. In this respect, modeling can be used for the prediction and optimization of the regimes, bringing matter under extreme thermodynamic conditions. In the next section, we discuss the routes of volumetric modification of transparent materials exposed to ultrashort DS laser pulses and demonstrate a possible scenario of the material dynamics after extreme energy coupling for the DS irradiation case, reported in ref. [30].

5. Possible Implications of Volumetric Modification of Transparent Dielectrics by Doughnut-Shaped Laser Pulses

Three scenarios of volumetric modification of transparent solids by focused DS laser pulses, for example, of fused silica, can be imagined with increasing pulse energy.

(i) At very low laser pulse energies, pulse-to-pulse defect accumulation leads to glass restructuring, accompanied by densification within the laser-affected zone, similar to that observed with UV glass aging [52]. Such regimes of modification require hundreds or even thousands of pulses coupling to the same material volume. The resulting structure can be seen in the form of a tube with a "wall" of a higher refractive index than the surrounding glass matrix. By slow longitudinal beam scanning [21], the final structure can plausibly represent a "hollow waveguide" imprinted in glass, although with lower contrast than in hollow fibers, in which the air is substituted by virgin glass.

(ii) At higher beam energies when glass exceeds the annealing point and approaches melting, fused silica enters the thermodynamic region, where its density increases with temperature [53]. Upon fast cooling, the glass is frozen in a compacted state characterized by a fictive temperature. This regime will presumably yield the same structure as in (i) but more optimally, with a smaller number of pulses and higher contrast in the refractive index.

(iii) A more complicated structure is formed by further increasing the laser beam energy when glass undergoes melting, with or without bubble formation. Under multi-pulse action with alternate melting and solidification within the laser-affected zone at low pulse repetition rates, or at high repetition rates of the order of 1 MHz, when the irradiated region is kept to be molten during irradiation, various defect-related zones [54,55] or, for multicomponent glasses, elemental separation can be achieved in a controlled way [56,57].

An attractive regime of irradiation within (iii) was predicted in ref. [30] in the formation of long tubular structures with hot "walls", which can produce an implosion of material with the creation of high-pressure phases when the material is brought into a highly non-equilibrium state. The swift formation of the hot-walled tubular structures inside transparent matter will initiate the generation of intriguing hydrodynamics, an example of which is shown below for the conditions of ref. [30].

In ref. [45], we applied thermoelastoplastic modeling to follow the evolution of laser-excited fused silica under action stress waves generated due to sudden volumetric heating by Gaussian laser pulses. The details of the model can be found in ref. [58]. We followed the dynamics of the stress waves and relocation of material with the creation of compacted and rarefied zones. Here, we applied this model to simulate the extreme conditions and the shock wave dynamics for the 2-μJ pulse (see ref. [30]). As the initial condition, the distribution of the absorbed laser energy was used, which was converted to the lattice temperature distribution based on thermodynamic relations [45]. The results of the modeling are presented in Figure 7. The laser beam propagated from the bottom. The geometrical focus in the simulations [30] was at z = 120 μm, while the main absorption of the DS pulses and, hence, the hydrodynamic effects developed well before the focus (see [30] for the details).

In the snapshot for 12 ps, the stress distribution is shown at which the material has not yet started to move. The compressive stress reaches the value of app. -0.4 TPa. Such stress levels can potentially induce transient [59] or permanent [60] formation of new phases and/or high-pressure material polymorphs. The snapshot for 50 ps demonstrates that the highly stressed cylindrical region emits two shock waves, one of which propagates to the periphery, similar to that generated by the Gaussian pulse [45], while the other one converges to the center of the laser-affected zone. The latter wave, upon its imploding to the center, reflects and starts to propagate to the periphery, thus following the first wave (the time moment of 100 ps in Figure 7). At this moment, the maximum pressure in the waves still exceeds 200 GPa. The stress level gradually decreases upon further propagation of the waves, dropping the maximum pressure to less than 100 GPa by the time of app. 650 ps. Interestingly, the velocity of the double wave propagation is ~16.5 km/s, in good

agreement with the experimental data on the fused silica Hugoniot using laser-driven shocks [61]. We remind the reader that the Rankine–Hugoniot relations describe the relationship between the states of a solid on two sides of a shock wave [62]. If the initial pressure and density are known, measurements of particle and shock velocities allow for the determination of equation-of-state. McCoy et al. [61] performed the measurements over a wide range of pressures from 200 to 1600 GPa. For 341 GPa and 393 GPa, the measured shock velocities were, respectively, 16.18 km/s and 17.25 km/s. This finding indicates that our thermoelastoplastic model catches very well the laser-induced shock wave formation and its propagation. Thus, by measuring the shock wave in dynamics [63], it is possible to determine the pressure level generated upon volumetric laser excitation of transparent materials. However, there are still open questions about the structural transformations that such a sequence of extremely strong shock waves can induce in materials, and whether such transformations are transient or they can permanently be frozen. Such research may offer new perspectives for gaining new knowledge about thermodynamic conditions in laser-irradiated, highly nonequilibrium matter.
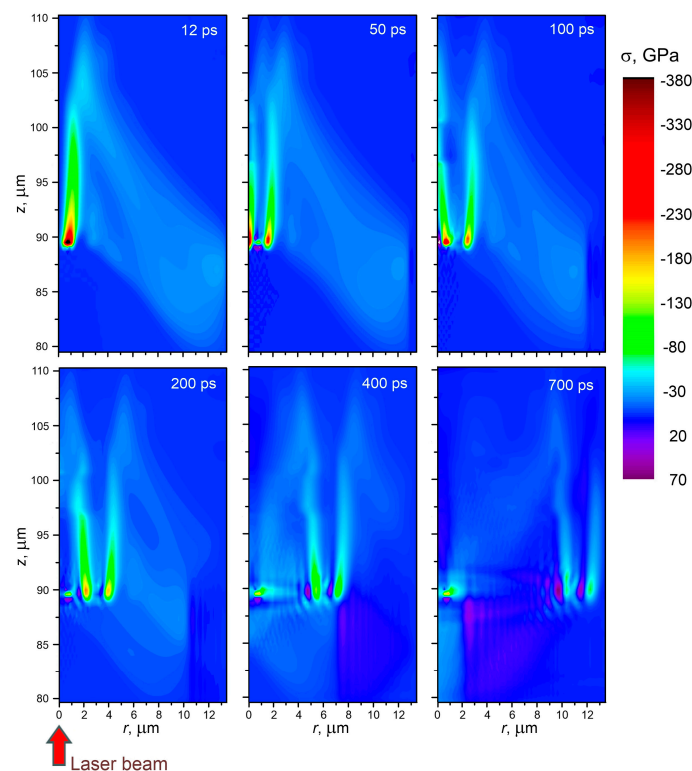
Figure 7. The dynamics of the double shock wave structure created in fused silica as the result of the action of the DS pulse with energy of 2 μJ for the conditions of laser excitation reported in ref. [30]. The laser beam propagates from the bottom. The geometrical focus is at $z = 120$ μm. The hydrodynamic effects develop in the regions well before the focus where the main absorption of the DS pulses occurs.

6. Conclusions

In this work, we investigated experimentally and theoretically the effect of the pulse shape of ultrashort laser excitation of fused silica in the regimes of volumetric modification. We focused on two shapes of the laser pulses: Gaussian and doughnut-shaped ones. It was found that, at relatively low pulse energies, in the range of ~1–5 μJ, the DS laser pulses are much more efficient in volumetric structural changes than Gaussian pulses, as predicted theoretically [30]. It is explained by the effect of intensity clamping for the Gaussian pulses, which leads to the delocalization of the laser energy absorption. In the DS case, this effect is overcome due to the geometry of the focused beam propagation, accompanied by the electron plasma formation, which scatters light toward the beam axis. However, it was also

found that, at beam energies of ~10 μJ and higher, the efficiency of the DS pulses drops, and at $E_p > 16$ μJ, the situation overturns, showing higher modification for the Gaussian pulses.

The thermoelastoplastic modeling performed for the DS pulses revealed an intriguing dynamic of the shock waves generated as a result of tubular energy absorption. We anticipate that such a double shock wave structure can induce the formation of high-pressure polymorphs of transparent materials and thus could be used for the investigation of the nonequilibrium thermodynamics of warm, dense matter, calling for further studies.

Author Contributions: Conceptualization, N.M.B.; methodology, M.Z. and N.M.B.; validation, M.Z., V.P.Z. and N.M.B.; formal analysis, V.P.Z. and Y.P.M.; Investigation, M.Z., V.P.Z., Y.P.M. and N.M.B.; resources, N.M.B.; data curation, M.Z. and N.M.B.; writing—original draft, M.Z., V.P.Z. and N.M.B.; writing—review and editing, M.Z., V.P.Z., Y.P.M. and N.M.B.; supervision, N.M.B.; funding acquisition, N.M.B. All authors have read and agreed to the published version of the manuscript.

Institutional Review Board Statement: Not applicable.

Informed Consent Statement: Not applicable.

Data Availability Statement: The data presented in this study are available on request from the corresponding author.

Dedication: This paper is our tribute to the memory of Alexander M. Rubenchik, our dear friend and teacher and an outstanding scientist, who inspired this work and provided very helpful comments.

References

1. Davis, K.M.; Miura, K.; Sugimoto, N.; Hirao, K. Writing waveguides in glass with a femtosecond laser. *Opt. Lett.* **1996**, *21*, 1729–1731. [CrossRef]
2. Homoelle, D.; Wielandy, S.; Gaeta, A.L.; Borrelli, N.F.; Smith, C. Infrared photosensitivity in silica glasses exposed to femtosecond laser pulses. *Opt. Lett.* **1999**, *24*, 1311–1313. [CrossRef]
3. Burakov, I.M.; Bulgakova, N.M.; Stoian, R.; Mermillod-Blondin, A.; Audouard, E.; Rosenfeld, A.; Husakou, A.; Hertel, I.V. Spatial distribution of refractive index variations induced in bulk fused silica by single ultrashort and short laser pulses. *J. Appl. Phys.* **2007**, *101*, 043506. [CrossRef]
4. Juodkazis, S.; Kohara, S.; Ohishi, Y.; Hirao, N.; Vailionis, A.; Mizeikis, V.; Saito, A.; Rode, A. Structural changes in femtosecond laser modified regions inside fused silica. *J. Opt.* **2010**, *12*, 124007. [CrossRef]
5. Alimohammadian, E.; Ertorer, E.; Uzeda, E.M.; Li, J.; Herman, P.R. Inhibition and enhancement of linear and nonlinear optical effects by conical phase front shaping for femtosecond laser material processing. *Sci. Rep.* **2020**, *10*, 21528. [CrossRef]
6. Kononenko, V.V.; Pashinin, V.P.; Komlenok, M.S.; Konov, V.I. Laser-induced modification of bulk fused silica by femtosecond pulses. *Laser Phys.* **2009**, *19*, 1294–1299. [CrossRef]
7. Canning, J.; Lancry, M.; Cook, K.; Weickman, A.; Brisset, F.; Poumellec, B. Anatomy of a femtosecond laser processed silica waveguide. *Opt. Mater. Express* **2011**, *1*, 998–1008. [CrossRef]
8. Cheng, G.H.; Lin, L.; Mishchik, K.; Stoian, R. Polarization-dependent scattering of nanogratings in femtosecond laser photowritten waveguides in fused silica. *Materials* **2022**, *15*, 5698. [CrossRef]
9. Ohfuchi, T.; Sakakura, M.; Yamada, Y.; Fukuda, N.; Takiya, T.; Shimotsuma, Y.; Miura, K. Polarization imaging camera with a waveplate array fabricated with a femtosecond laser inside silica glass. *Opt. Express* **2017**, *25*, 23738–23754. [CrossRef] [PubMed]
10. Tian, J.; Yao, H.; Cavillon, M.; Garcia-Caure, E.; Ossikovski, R.; Stchakovsky, M.; Eypert, C.; Poumellec, B.; Lancry, M. A comparison between nanogratings-based and stress-engineered waveplates written by femtosecond laser in silica. *Micromachines* **2020**, *11*, 131. [CrossRef] [PubMed]
11. Mihailov, S.J.; Smelser, C.W.; Grobnic, D.; Walker, R.B.; Lu, P.; Ding, H.M.; Unruh, J. Bragg gratings written in all-SiO$_2$ and Ge-doped core fibers with 800-nm femtosecond radiation and a phase mask. *J. Light. Technol.* **2004**, *22*, 94–100. [CrossRef]
12. Martinez, A.; Dubov, M.; Khrushchev, I.; Bennion, I. Direct writing of fibre Bragg gratings by femtosecond laser. *Electron. Lett.* **2004**, *40*, 1170–1172. [CrossRef]
13. Li, H.; Yang, B.; Wang, M.; Gao, C.; Wu, B.; Zeng, L.; Xi, X.; Chen, Z.; Wang, X.; Wang, Z.; et al. Femtosecond laser fabrication of large-core fiber Bragg gratings for high-power fiber oscillators. *APL Photonics* **2023**, *8*, 046101. [CrossRef]
14. Glezer, E.N.; Milosavljevic, M.; Huang, L.; Finlay, R.J.; Her, T.-H.; Callan, J.P.; Mazur, E. Three-dimensional optical storage inside transparent materials. *Opt. Lett.* **1996**, *21*, 2023–2025. [CrossRef] [PubMed]

15. Qiu, J.R.; Miura, K.; Hirao, K. Three-dimensional optical memory using glasses as a recording medium through a multi-photon absorption process. *Jpn. J. Appl. Phys.* **1998**, *37*, 2263–2266. [CrossRef]
16. Shimotsuma, Y.; Sakakura, M.; Kazansky, P.G.; Beresna, M.; Qiu, J.R.; Miura, K.; Hirao, K. Ultrafast manipulation of self-assembled form birefringence in glass. *Adv. Mater.* **2010**, *22*, 4039–4043. [CrossRef]
17. Cai, W.J.; Libertun, A.R.; Piestun, R. Polarization selective computer-generated holograms realized in glass by femtosecond laser induced nanogratings. *Opt. Express* **2006**, *14*, 3785–3791. [CrossRef]
18. Sugioka, K.; Cheng, Y. Femtosecond laser processing for optofluidic fabrication. *Lab Chip* **2012**, *12*, 3576–3589. [CrossRef]
19. Sima, F.; Sugioka, K.; Vazquez, R.M.; Osellame, R.; Kelemen, L.; Ormos, P. Three-dimensional femtosecond laser processing for lab-on-a-chip applications. *Nanophotonics* **2018**, *7*, 613–634. [CrossRef]
20. Diez-Blanco, V.; Siegel, J.; Ferrer, A.; de la Cruz, A.R.; Solis, J. Deep subsurface waveguides with circular cross section produced by femtosecond laser writing. *Appl. Phys. Lett.* **2007**, *91*, 051104. [CrossRef]
21. Mermillod-Blondin, A.; Burakov, I.M.; Meshcheryakov, Y.P.; Bulgakova, N.M.; Audouard, E.; Rosenfeld, A.; Husakou, A.; Hertel, I.V.; Stoian, R. Flipping the sign of refractive index changes in ultrafast-laser-irradiated borosilicate crown optical glass at high repetition rates. *Phys. Rev. B* **2008**, *77*, 104205. [CrossRef]
22. Zambon, V.; McCarthy, N.; Piché, M. Laser micromachining of transparent glass using ultrafast Bessel beams. In Proceedings of the Photonics North 2009, Montréal, QC, USA, 24–27 May 2009; Volume 7386, p. 738632. [CrossRef]
23. Courvoisier, F.; Stoian, R.; Couairon, A. Ultrafast laser micro- and nano-processing with nondiffracting and curved beams. *Opt. Laser Technol.* **2016**, *80*, 125–137. [CrossRef]
24. Shen, T.; Tian, D.; Chen, T.; Li, P.; Hou, X. The spatiotemporal dynamics of electron plasma in femtosecond laser double pulses induced damage in fused silica. *Photonics* **2023**, *10*, 702. [CrossRef]
25. Paipulas, D.; Mikutis, M.; Sirutkaitis, V.; Juodkazis, S. Volumetric modifications in fused silica using Gaussian and Bessel femtosecond laser beams. In *Pacific Rim Laser Damage 2013: Optical Materials for High Power Lasers*; SPIE: Paris, France, 2013; Volume 8786, pp. 66–73. [CrossRef]
26. Vetter, C.; Giust, R.; Furfaro, L.; Billet, C.; Froehly, L.; Courvoisier, F. High aspect ratio structuring of glass with ultrafast Bessel beams. *Materials* **2021**, *14*, 6749. [CrossRef] [PubMed]
27. Ardaneh, K.; Giust, R.; Charpin, P.-J.; Morel, B.; Courvoisier, F. Electron heating and radiation in high aspect ratio sub-micron plasma generated by an ultrafast Bessel pulse within a solid dielectric. *Eur. Phys. J. Spec. Top.* **2022**. [CrossRef]
28. Le, H.; Penchev, P.; Henrottin, A.; Bruneel, D.; Nasrollahi, V.; Ramos-de-Campos, J.A.; Dimov, S. Effects of top-hat laser beam processing and scanning strategies in laser micro-structuring. *Micromachines* **2020**, *11*, 221. [CrossRef] [PubMed]
29. Möhl, A.; Kaldun, S.; Kunz, C.; Müller, F.A.; Fuchs, U.; Gräf, S. Tailored focal beam shaping and its application in laser material processing. *J. Laser Appl.* **2019**, *31*, 042019. [CrossRef]
30. Zhukov, V.P.; Rubenchik, A.M.; Fedoruk, M.P.; Bulgakova, N.M. Interaction of doughnut-shaped laser pulses with glasses. *J. Opt. Soc. Am. B* **2017**, *34*, 463–471. [CrossRef]
31. Couairon, A.; Mysyrowicz, A. Femtosecond filamentation in transparent media. *Phys. Rep.* **2007**, *441*, 47–189. [CrossRef]
32. Gildenburg, V.B.; Pavlichenko, I.A. High contrast periodic plasma pattern formation during the laser-induced breakdown in transparent dielectric. *Phys. Plasmas* **2017**, *24*, 122306. [CrossRef]
33. Bulgakova, M.M.; Zhukov, V.P.; Meshcheryakov, Y.P.; Gemini, L.; Brajer, J.; Rostohar, D.; Mocek, T. Pulsed laser modification of transparent dielectrics: What can be foreseen and predicted by numerical simulations? *J. Opt. Soc. Am. B* **2014**, *31*, C8–C14. [CrossRef]
34. Itoh, C.; Tanimura, K.; Itoh, N. Optical studies of self-trapped excitons in SiO_2. *J. Phys. C Solid State Phys.* **1988**, *21*, 4693–4702. [CrossRef]
35. Audebert, P.; Daguzan, P.; Dos Santos, A.; Gauthier, J.C.; Geindre, J.P.; Guizard, S.; Hamoniaux, G.; Krastev, K.; Martin, P.; Petite, G.; et al. Space-time observation of an electron gas in SiO_2. *Phys. Rev. Lett.* **1994**, *73*, 1990–1993. [CrossRef] [PubMed]
36. Grojo, D.; Gertsvolf, M.; Lei, S.; Barillot, T.; Rayner, D.M.; Corkum, P.B. Exciton-seeded multiphoton ionization in bulk SiO_2. *Phys. Rev. B* **2010**, *81*, 212301. [CrossRef]
37. Kaiser, A.; Rethfeld, B.; Vicanek, M.; Simon, G. Microscopic processes in dielectrics under irradiation by subpicosecond laser pulses. *Phys. Rev. B* **2000**, *61*, 11437–11450. [CrossRef]
38. Martin, P.; Guizard, S.; Daguzan, P.; Petite, G.; D'Oliveira, P.; Meynadier, P.; Perdrix, M. Subpicosecond study of carrier trapping dynamics in wide-band-gap crystals. *Phys. Rev. B* **1997**, *55*, 5799. [CrossRef]
39. Bulgakova, N.M.; Zhukov, V.P.; Meshcheryakov, Y.P. Theoretical treatments of ultrashort pulse laser processing of transparent materials: Towards understanding the volume nanograting formation and "quill" writing effect. *Appl. Phys. B* **2013**, *113*, 437–449. [CrossRef]
40. Zhukov, V.P.; Fedoruk, M.P. Numerically implemented impact of a femtosecond laser pulse on glass in the approximation of nonlinear Maxwell equations. *Math. Models Comput. Simul.* **2020**, *12*, 77–89. [CrossRef]
41. Popov, K.I.; Bychenkov, V.Y.; Rozmus, W.; Sydora, R.D.; Bulanov, S.S. Vacuum electron acceleration by tightly focused laser pulses with nanoscale targets. *Phys. Plasmas* **2009**, *16*, 053106. [CrossRef]
42. Couairon, A.; Kosareva, O.G.; Panov, N.A.; Shipilo, D.E.; Andreeva, V.A.; Jukna, V.; Nesa, F. Propagation equation for tight-focusing by a parabolic mirror. *Opt. Express* **2015**, *23*, 31240–31252. [CrossRef]
43. Stratton, J.A.; Chu, L.J. Diffraction Theory of Electromagnetic Waves. *Phys. Rev.* **1939**, *56*, 99. [CrossRef]

44. Zhukov, V.P.; Fedoruk, M.P. High efficient method for calculation of Stratton-Chu integral in problems of interaction of laser radiation with materials. *Comput. Technol.* **2021**, *26*, 42–60. [CrossRef]

45. Bulgakova, N.M.; Zhukov, V.P.; Sonina, S.V.; Meshcheryakov, Y.P. Modification of transparent materials with ultrashort laser pulses: What is energetically and mechanically meaningful? *J. Appl. Phys.* **2015**, *118*, 233108. [CrossRef]

46. Zavedeev, E.V.; Kononenko, V.V.; Gololobov, V.M.; Konov, V.I. Modeling the effect of fs light delocalization in Si bulk. *Laser Phys. Lett.* **2014**, *11*, 036002. [CrossRef]

47. Liu, V.I.; Petit, S.; Becker, A.; Aközbek, N.; Bowden, C.M.; Chin, S.L. Intensity clamping of a femtosecond laser pulse in condensed matter. *Opt. Commun.* **2002**, *202*, 189–197. [CrossRef]

48. Sun, Q.; Liang, F.; Vallee, R.; Chin, S.L. Nanograting formation on the surface of silica glass by scanning focused femtosecond laser pulses. *Opt. Lett.* **2008**, *33*, 2713–2715. [CrossRef] [PubMed]

49. Stoian, R.; Bonse, J. (Eds.) Ultrafast Laser Nanostructuring: The Pursuit of Extreme Scales. In *Springer Series in Optical Sciences*; Springer: Cham, Switzerland, 2023. [CrossRef]

50. Schultze, M.; Bothschafter, E.M.; Sommer, A.; Holzner, S.; Schweinberger, W.; Fiess, M.; Hofstetter, M.; Kienberger, R.; Apalkov, V.; Yakovlev, V.S.; et al. Controlling dielectrics with the electric field of light. *Nature* **2012**, *493*, 75–78. [CrossRef] [PubMed]

51. Derrien, T.J.-Y.; Tancogne-Dejean, N.; Zhukov, V.P.; Appel, H.; Rubio, A.; Bulgakova, N.M. Photoionization and transient Wannier-Stark ladder in silicon: First-principles simulations versus Keldysh theory. *Phys. Rev. B* **2021**, *104*, L241201. [CrossRef]

52. Borrelli, N.F.; Smith, C.; Allan, D.C.; Seward, T.P. Densification of fused silica under 193-nm excitation. *J. Opt. Soc. Am. B* **1997**, *14*, 1606–1615. [CrossRef]

53. Brückner, R. Properties and structure of vitreous silica. I. *J. Non-Cryst. Solids* **1070**, *5*, 123–175. [CrossRef]

54. Kazansky, P.G.; Shimotsuma, Y.; Sakakura, M.; Beresna, M.; Gecevičius, M.; Svirko, Y.; Akturk, S.; Qiu, J.; Miura, K.; Hirao, K. Photosensitivity control of an isotropic medium through polarization of light pulses with tilted intensity front. *Opt. Express* **2011**, *19*, 20657–20664. [CrossRef]

55. Zhang, F.; Xie, X.; Zhao, X.; Ma, L.; Lei, L.; Qiu, J.; Nie, Z. Polarization-dependent microstructural evolution induced by a femtosecond laser in an aluminosilicate glass. *Opt. Express* **2021**, *29*, 10265–10274. [CrossRef] [PubMed]

56. Sakakura, M.; Yoshimura, K.; Kurita, T.; Shimizu, M.; Shimotsuma, Y.; Fukuda, N.; Hirao, K.; Miura, K. Condensation of Si-rich region inside soda-lime glass by parallel femtosecond laser irradiation. *Opt. Express* **2014**, *22*, 16493–16503. [CrossRef] [PubMed]

57. Macias-Montero, M.; Muñoz, F.; Sotillo, B.; del Hoyo, J.; Ariza, R.; Fernandez, P.; Siegel, J.; Solis, J. Femtosecond laser induced thermophoretic writing of waveguides in silicate glass. *Sci. Rep.* **2021**, *11*, 8390. [CrossRef] [PubMed]

58. Meshcheryakov, Y.P.; Shugaev, M.V.; Mattle, T.; Lippert, T.; Bulgakova, N.M. Role of thermal stresses on pulsed laser irradiation of thin films under conditions of microbump formation and non-vaporization forward transfer. *Appl. Phys. A* **2013**, *113*, 521. [CrossRef]

59. Gleason, A.E.; Bolme, C.A.; Lee, H.J.; Nagler, B.; Galtier, E.; Milathianaki, D.; Hawreliak, J.; Kraus, R.G.; Eggert, J.H.; Fratanduono, D.E.; et al. Ultrafast visualization of crystallization and grain growth in shock-compressed SiO_2. *Nat. Commun.* **2015**, *6*, 8191. [CrossRef] [PubMed]

60. Vailionis, A.; Gamaly, E.G.; Mizeikis, V.; Yang, W.; Rode, A.V.; Juodkazis, S. Evidence of superdense aluminium synthesized by ultrafast microexplosion. *Nat. Commun.* **2011**, *2*, 445. [CrossRef] [PubMed]

61. McCoy, C.A.; Gregor, M.C.; Polsin, D.N.; Fratanduono, D.E.; Celliers, P.M.; Boehly, T.R.; Meyerhofer, D.D. Shock-wave equation-of-state measurements in fused silica up to 1600 GPa. *J. Appl. Phys.* **2016**, *119*, 215901. [CrossRef]

62. Zukas, J.A. Shock waves in solids. In *Studies in Applied Mechanics*; Elsevier: Amsterdam, The Netherlands, 2004; Volume 49, Chapter 3; pp. 75–102. [CrossRef]

63. Sakakura, M.; Shimotsuma, Y.; Miura, K. Observation of stress wave and thermal stress in ultrashort pulse laser bulk processing inside glass. *J. Laser Micro Nanoeng.* **2017**, *12*, 159–164. [CrossRef]